High strain rate effects in masonry structures under waterborne debris impacts

Alessandro De Iasio [a],[*], Bahman Ghiassi [b], Riccardo Briganti [a], Gabriele Milani [c]

[a] Environmental Fluid Mechanics and Geoprocesses, Department of Civil Engineering, Faculty of Engineering, University Park, NG7 2RD Nottingham, United Kingdom
[b] Department of Civil Engineering, University of Birmingham, B15 2TT, United Kingdom
[c] Department of Architecture Built Environment and Construction Engineering (ABC), Politecnico di Milano, Piazza Leonardo da Vinci 32, 20133 Milan, Italy

ARTICLE INFO

ABSTRACT

Masonry buildings are vulnerable to extreme hydrodynamic events such as floods or tsunamis. Post-disaster surveys have shown that waterborne debris impacts can significantly damage masonry walls during these events. To simulate these actions, the current design or research practice is to compute the force–time diagram of the impact and then use it for dynamic analyses. Standing on the current knowledge, debris impacts are highly impulsive, but it is not clear if such loads are fast enough to activate the high strain rate effects in masonry, i.e. the strain rate dependency of material properties. The present study aims to answer this question, for the first time, following nonlinear Finite Element (FE) simulations. Simulations are conducted on a masonry wall, following a micro-modelling strategy, subjected to water flow and waterborne debris impact under different scenarios. It is found that the strain rates exceed the critical threshold after which strain rate effects are considerable. Such a finding, initially obtained using the minimum design demand for log-type debris imposed by ASCE/SEI 7-22, is further extended to a range of impact force–time diagrams different in impact duration and peak force (corresponding to different debris properties or flow velocity). It is also shown that the impact location (i.e. midspan or close to the boundary) affects the strain rate magnitude because of the changes in the impact stiffness and the activated failure mechanisms. Furthermore, it is found that the dynamic tensile post-elastic behaviour of the materials is the most influencing parameter in the structural response. These results open a new area in the field of assessment and design of masonry structures to waterborne debris and guide the development of future experiments, numerical simulations or design relations.

1. Introduction

Residential masonry buildings are widely used in many countries. In the case of extreme hydrodynamic events, like tsunamis or floods, such structures are highly vulnerable as post-disaster surveys show that masonry walls can collapse under water pressure [46,25]. In cases where the structure resists the flow actions, significant damage can still occur due to waterborne debris impacts [25]. With the increasing frequency of extreme hydrodynamic events due to climate change [49], there is a critical need to understand masonry structural response during such events. This need motivates the present study.

The current engineering practice, including design provisions by ASCE/SEI 7-22 [3], to model debris impacts is based on calculating the impact force–time diagram with a simplified analytical model, e.g. the impulse-momentum [15] or the contact-stiffness [35], and using it in a dynamic structural analysis. However, the research supporting this practice is limited and mainly focused on the response to flow actions only. Previous studies have confirmed the high vulnerability of masonry walls to combinations of water depth and velocity associated with these events, i.e. $1m$ depth and $2m/s$ speed, using nonlinear macro (i.e. homogenised masonry representation) Finite Elements (FE) models or Limit Analysis (LA) procedures applied to homogenised masonry rigid blocks [33,7,21]. Regarding the waterborne debris impacts, however, experiments are still unavailable according to the author's knowledge. Numerical studies are more developed, although also limited. Some authors have studied the occurrence of debris impact on masonry walls using an elastic macro FE model and computing the impact force with the impulse-momentum model [20,19,48]. Others have used Smoothed Particle Hydrodynamic (SPH) simulations to quantify the hydrodynamic

* Corresponding author.
  E-mail addresses: alessandro.deiasio@nottingham.ac.uk (A. De Iasio), b.ghiassi@bham.ac.uk (B. Ghiassi), riccardo.briganti@nottingham.ac.uk (R. Briganti), gabriele.milani@polimi.it (G. Milani).

Nomenclature

A_d	Log debris cross-section area
b/w	Blocking ratio
C_{hd}	Drag coefficient
C_p	Pressure coefficient
d	Wall horizontal displacement
DIF	Dynamic Increase Factor
E	Young's modulus
f_C	Cut-off frequency
F_d	Debris impact force
Fr	Froude number
g	Gravity acceleration
G_f^t	Tensile fracture energy
G_f^c	Compressive fracture energy
h_w	Water depth
l_{ec}	Finite element characteristic length
K_c	Ratio of the biaxial to uniaxial compressive yield stresses
k_d	Debris stiffness
k_{eff}	Effective elastic impact stiffness
k_s	Structure stiffness
l_d	Debris length
m_d	Debris weight
p	Pressure on the wall surface
q_{hd}	Hydrodynamic pressure
q_{hs}	Maximum hydrostatic pressure
s	Mesh size control parameter
t_d	Debris impact duration
v_d	Debris velocity
v_w	Flow velocity
δ	Crack width
Δt	Simulation time increment
$\in$	Eccentricity parameter
ε	Strain
$\widehat{\varepsilon}_{max}$	Maximum principal strain
$\widehat{\varepsilon}_{min}$	Minimum principal strain
ε_t^{ck}	Tensile cracking strain
$\widetilde{\varepsilon}_c^{pl}$	Compressive equivalent plastic strain
$\widetilde{\varepsilon}_t^{pl}$	Tensile equivalent plastic strain
$\dot{\varepsilon}_{c,i}^{inst}$	Instantaneous rate of the minimum principal strain
$\dot{\varepsilon}_{t,i}^{inst}$	Instantaneous rate of the maximum principal strain
$\dot{\varepsilon}_c$	Filtered rate of the minimum principal strain
$\dot{\varepsilon}_t$	Filtered rate of the maximum principal strain
μ	Viscosity parameter
ν	Poisson's ratio
ρ	Material density
ρ_w	Fluid density
ρ_d	Debris density
σ	Stress
$\widehat{\sigma}_{max}$	Maximum principal stress
$\widehat{\sigma}_{mid}$	Medium principal stress
$\widehat{\sigma}_{min}$	Minimum principal stress
σ_{b0}	Biaxial compressive yield stress
σ_c	Uniaxial compressive strength
σ_{c0}	Uniaxial compressive yield stress
σ_t	Uniaxial tensile strength
φ_d	Log debris cross-section diameter
ψ	Dilation angle
ω	Smoothing factor for filtering

and debris impact forces on a rigid masonry arch bridge [32,31] and eventually applied those forces to a nonlinear FE macro model of the same structure [31]. All of these studies highlighted that debris impacts cause a significant stress concentration at the collision point and cracking of masonry, but, also due to the low level of details of their models, none of these analysed the mechanic of the local failures. As the debris impact loads are characterised by force–time diagrams with a duration in the order of $10^{-2}s$ and peak force in the order of $10^5 N$ [35,39], such loads can be highly impulsive. Therefore, it is possible that debris impacts on masonry structures activate the strain rate effects in the masonry constituents, i.e. the strain rate dependency of material properties when such rates pass a certain threshold [17]. However, the literature does not contain any investigations into this possibility, with consequent uncertainties about the reliability of simulations currently neglecting them. Moreover, in case the rate effects are activated, it is unknown if some of the rate-dependent material properties affect the structural response more than others, with possible implications in optimising the DIF data collection process in experimental campaigns.

In this paper, we aim, for the first time, to investigate the strain rate effects in masonry structures under waterborne debris impacts. In particular, we want to demonstrate whether such impulsive loads can cause strain rates high enough to activate the high strain rate effects in masonry, if the impact location affects the strain rate values and if there are material properties which are more involved than others in the rate-dependent response. A Finite Element (FE) modelling strategy, validated with experimental results, is followed to answer this research question. The simulations are focused on an individual masonry wall represented following a micro-modelling approach (i.e. detailed masonry representation), which we introduce for the first time in the field of debris impacts on masonry and that opens the possibility of investigating the mechanic of the local failures in detail. The wall is subjected to the flow

actions and debris impact load, firstly as recommended by ASCE/SEI 7-22, then investigating how different debris and flow properties influence the strain rate effects. The flow is assumed in subcritical conditions as it is more relevant to such natural hazards that can lead to debris transport [37]. Also, as such scenarios are less aggressive, the general belief is that the waterborne debris impacts are less severe in such scenarios, the accuracy of which is under interrogation in the presented paper. The material models consider the strain rate dependent properties using a set of experimental Dynamic Increase Factors (DIF). The results are presented and discussed in terms of strain rates introduced to the wall under different impact loading scenarios and their effects on the structural response, i.e. displacements and crack patterns.

The structure of the paper is as follows. Section 2 describes the structural model. Section 3 defines applied load, their modelling and the input parameters. Finally, Section 4 presents the results and their discussion. Conclusions are drawn in Section 5.

2. Structural model

2.1. Masonry micro-model

The model of a masonry wall is created in the FE software Abaqus/CAE 2018 [1] by adopting a 3D micro-modelling strategy to simulate local failures accurately. Bricks and mortar are modelled individually as nonlinear materials, assuming a perfect bond along their interfaces [45]. The materials are considered isotropic at the Gauss points. The elastic behaviour is defined by Young's modulus E and Poisson's ratio ν, and the post-yield response is simulated with the Concrete Damage Plasticity (CDP) model, which is widely used in the masonry field [14]. The yield surfaces are adapted from Lubliner et al. [30] and Lee and Fenves [26]. A non-associated potential plastic flow based on a Drucker-Prager

hyperbolic function is used. The plasticity input parameters are the dilation angle ψ, the eccentricity parameter ϵ, the ratio of the biaxial to uniaxial compressive yield stresses σ_{bo}/σ_{c0}, the ratio between the second stress invariant on the tensile meridian to that on the compressive meridian K_c and the viscosity parameter μ. The material behaviour is defined with uniaxial compressive and tensile stress–strain laws. A softening branch is included to model material cracks and to simulate the degradation of the structure stiffness during the analysis. The equivalent plastic strains in compression ($\tilde{\varepsilon}_{pl}^c$) and tension ($\tilde{\varepsilon}_{pl}^t$) are the internal hardening variables, which are functions of the principal stresses and strains and define the post-yield status at Gauss points. The strain rate dependence of material properties is also implemented (see Section 2.3).

2.2. Materials constitutive laws

The post-elastic uniaxial compressive behaviour of bricks and mortar is represented by the parabolic model proposed by Feenstra [13] for plain concrete and validated for masonry constituents by Drougkas et al. [12]. The expression is:

$$\sigma(\varepsilon) = \begin{cases} \dfrac{\sigma_c}{3}\left(1 + 4\left(\dfrac{\varepsilon - \varepsilon_{c,3}}{\varepsilon_c - \varepsilon_{c,3}}\right) - 2\left(\dfrac{\varepsilon - \varepsilon_{c,3}}{\varepsilon_c - \varepsilon_{c,3}}\right)^2\right), \varepsilon_{c,3} \leq \varepsilon < \varepsilon_c \\[2ex] \dfrac{\sigma_c}{3}\left(1 - \left(\dfrac{\varepsilon - \varepsilon_c}{\varepsilon_u - \varepsilon_c}\right)^2\right), \varepsilon_c \leq \varepsilon < \varepsilon_u \\[2ex] 0, \varepsilon \geq \varepsilon_u \end{cases} \quad (1)$$

where ε is the total strain, σ is the stress, σ_c is the compressive strength, and

$$\varepsilon_{c,3} = \frac{1}{3}\frac{\sigma_c}{E}, \ \varepsilon_c = \frac{5}{3}\frac{\sigma_c}{E}, \ \varepsilon_u = \varepsilon_c + \frac{3}{2}\frac{G_f^c}{l_{ec}\sigma_c} \quad (2)$$

where G_f^c is the compressive fracture energy, $\varepsilon_{c,3}$ is the loss of linearity strain, ε_c is the strain at peak and ε_u is the ultimate strain. G_f^c is the compressive fracture energy, which is computed as:

$$G_f^c = d\sigma_c \quad (3)$$

where d is a ductility parameter, which is recommended equal to $1mm$ for both bricks and mortar [12]. Finally, l_{ec} is the characteristic element length, which is used to remove the mesh sensitivity due to the lower dissipated energy upon mesh refinement that is usually observed in nonlinear FE simulations. This method, called the Crack Band Method [5], assumes that a crack occurs along a single-element layer. l_{ec} is the ratio between the volume and the largest face area for linear elements or half of it for quadratic ones [2].

The post-elastic uniaxial tensile behaviour of bricks and mortar is represented by the exponential softening curve proposed by Hordijk [18] for plain concrete and is validated for bricks and mortar by Pluijm [40]. The expression is:

$$\sigma(w) = \sigma_t\left\{\left[1 + \left(c_1\frac{w}{w_c}\right)^3\right]e^{-c_2\frac{w}{w_c}} - \frac{w}{w_c}\left(1 + c_1^3\right)e^{-c_2}\right\} \quad (4)$$

where w is the crack width, σ_t is the tensile strength, $c_1 = 3$, $c_2 = 6.93$ and $w_c = 5.14 \bullet G_f^t/\sigma_t$. G_f^t is the tensile fracture energy. To convert the stress-displacement curve (Eq. (4)) to the stress-cracking strain one required as input, the cracking strain (ε_t^{ck}) is computed as in Alfarah et al. [2]:

$$\varepsilon_t^{ck} = \frac{w}{l_{ec}} \quad (5)$$

Finally, the tensile fracture energy is computed as in Ghiassi and Milani [14]:
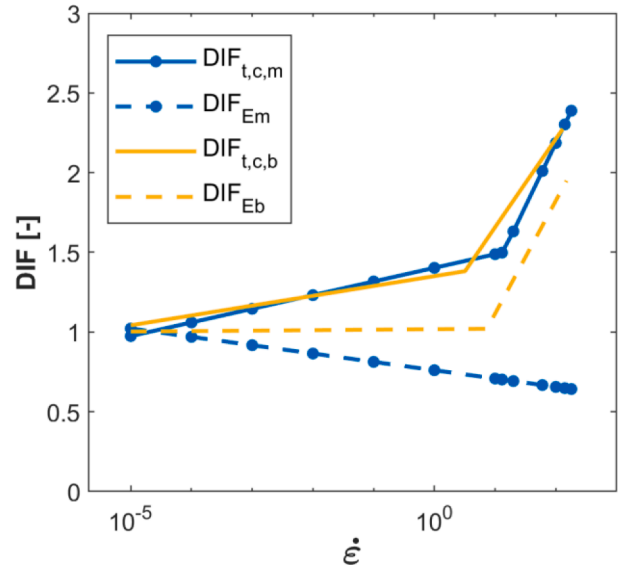

Fig. 1. DIF equations as a function of the strain rate by Hao and Tarasov [17].

$$G_f^t = 0.025\left(\frac{\sigma_c}{10}\right)^{0.7} \quad (6)$$

where G_f^t and σ_c are expressed in N/mm and MPa, respectively.

2.3. Strain rate effects

The strain rate effects are included using rate-dependent material properties, also called dynamic properties. These are obtained by multiplying the static properties for the related Dynamic Increase Factors (DIF), which express the ratios of the dynamic to the static parameters as functions of the strain rate. The DIF are applied to E for the elastic behaviour, to σ_t and G_f^t for the post-elastic tensile behaviour and to σ_c and G_f^c for the post-elastic compressive behaviour. The DIF equations by Hao and Tarasov [17] for σ_c and E for bricks and mortar are used (see Eqs. 7–10 and Fig. 1. These equations show that the critical threshold to have significant high strain rate effects is in a range between $1s^{-1}$ and $10s^{-1}$. In the absence of specific data for the dynamic tensile strength, the DIF of σ_c is used for σ_t [43,47]. The same is done for G_f^c and G_f^t, for which the same DIF of the strength are used [4]. Referring to the tensile post-elastic behaviour with the subscript t and the compressive post-elastic one with c, and to the mortar with m and bricks with b, the expression used for the mortar behaviours is:

$$DIF_{t,m} = DIF_{c,m} = \begin{cases} 0.0372\ \ln(\dot{\varepsilon}) + 1.4025 & 2 \times 10^{-5}s^{-1} < \dot{\varepsilon} < 13s^{-1} \\ 0.3447\ \ln(\dot{\varepsilon}) + 0.5987 & 13s^{-1} < \dot{\varepsilon} < 200s^{-1} \end{cases}$$
$$(7)$$

The expression for E_m is:

$$DIF_{Em} = -0.02272\ \ln(\dot{\varepsilon}) + 0.7601 \qquad 2 \times 10^{-5}s^{-1} < \dot{\varepsilon} < 13s^{-1} \quad (8)$$

The expression for the bricks tensile (t) and compressive (c) behaviours is:

$$DIF_{t,b} = DIF_{c,b} = \begin{cases} 0.0268\ \ln(\dot{\varepsilon}) + 1.3504 & 2 \times 10^{-6}s^{-1} < \dot{\varepsilon} < 3.2s^{-1} \\ 0.2405\ \ln(\dot{\varepsilon}) + 1.1041 & 3.2s^{-1} < \dot{\varepsilon} < 150s^{-1} \end{cases}$$
$$(9)$$

The expression for the E_b is:

$$DIF_{Eb} = \begin{cases} 0.0013\ \ln(\dot{\varepsilon}) + 1.0174 & 2 \times 10^{-6}s^{-1} < \dot{\varepsilon} < 7.3s^{-1} \\ 0.3079\ \ln(\dot{\varepsilon}) + 0.4063 & 7.3s^{-1} < \dot{\varepsilon} < 150s^{-1} \end{cases}$$
$$(10)$$

The dynamic material laws are implemented using a VUSDFLD
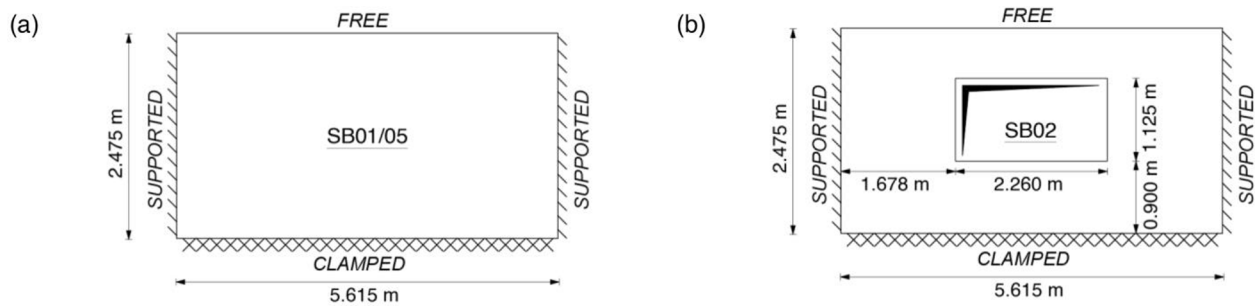
Fig. 2. Walls geometry and boundary conditions [8]: (a) SB01/05 and (b) SB02.

Fortran subroutine [1]. In this subroutine, the strain rates are continuously computed at each Gauss point during the analysis and used for calculating the DIF values according to Eqs. (7–10) to update the mechanical properties. The rates are computed backwards at the beginning of the ith time step, based on the values of the ith and the $(i-1)^{th}$ steps, separated by a time interval of Δt_i. The instantaneous strain rates for tension, $\dot{\varepsilon}_{t,i}^{inst}$, and compression, $\dot{\varepsilon}_{c,i}^{inst}$, are calculated as:

$$\dot{\varepsilon}_{t,i}^{inst} = \frac{\widehat{\varepsilon}_{max,i} - \widehat{\varepsilon}_{max,i-1}}{\Delta t_i}, \dot{\varepsilon}_{c,i}^{inst} = \frac{\widehat{\varepsilon}_{min,i} - \widehat{\varepsilon}_{min,i-1}}{\Delta t_i} \quad (11)$$

where $\widehat{\varepsilon}_{max}$ and $\widehat{\varepsilon}_{min}$ are the maximum and minimum principal strains, respectively. However, the $\dot{\varepsilon}_{t,i}^{inst}$ and $\dot{\varepsilon}_{c,i}^{inst}$ values cannot be used directly because of the presence of high-frequency oscillations, which introduce spurious damage to the structure and lead to inaccurate results [27]. Therefore, the strain rates are filtered to obtain $\dot{\varepsilon}_{k,i}$ by applying the following equation [27]:

$$\dot{\varepsilon}_{k,i} = \omega \dot{\varepsilon}_{k,i}^{inst} + (1 - \omega) \dot{\varepsilon}_{k,i-1} \quad (12)$$

where the subscript k is represented as c (if compression) or t (if tension), and ω is the smoothing factor, which is computed as in Cahuzac et al. [6]:

$$\omega = \frac{2\pi f_c \Delta t_i}{\sqrt{3}} \quad (13)$$

where f_c is the cut-off frequency. As the frequency of non-physical oscillations is unknown, a sensitivity analysis is conducted to identify the best value for f_c (see Section 4.1)

It is worth noting some features of the strain rate effects modelling. First, the strain rate effects are not considered in the unloading phase, as there is no evidence that different unloading speeds change the material behaviour. Second, E is unique at the integration points as isotropic materials are used (see Section 2.1), thus, it can be associated with one strain rate value only. The literature does not specify a methodology for this, so either $\dot{\varepsilon}_t$ and $\dot{\varepsilon}_c$ are used, and their results are compared (see Section 4.3). Finally, upon reaching a plastic strain threshold, here selected as 1% of the static peak stress equal to that proposed by Abaqus to ensure numerical stability [1], the elements are deemed to have failed. Consequently, the strain rates are fixed to zero in those elements to avoid obtaining fictitious maximum rates. Preliminary analyses showed that the maximum rates are overestimated by up to 50% in some cases if this procedure is not followed.

2.4. Model validation

The structural model is validated with the experimental tests by Chong [8] on the SB01/05 and SB02 walls (Fig. 2). These are running bond masonry walls of $5.615m$ wide and $2.475m$ tall. The bricks are $215 \times 102.5 \times 65mm^3$ fired-clay bricks, bonded by $10mm$ thick cement: lime:sand (1:1:6 in volume) mortar joints. The base is fixed, the vertical edges are simply supported, and the top edge is free. SB01/05 has no

Table 1
Mechanical properties of bricks and mortar selected for simulating walls SB01/05 and SB02.

Parameter	Bricks	Source	Mortar	Source
$\rho[\text{kg/m}^3]$	1590	[8]	2113	[8]
$E[\text{MPa}]$	16,700	[29]	4000	[23]
$\nu[-]$	0.20	[29]	0.20	[29]
$\sigma_c[\text{MPa}]$	38.20	[8]	11.50	[8]
$G_f^c[\text{N/m}]$	38,200	Eq. (3)	11,500	Eq. (3)
$\sigma_t[\text{MPa}]$	3.82	[14]	0.58	[28]
$G_f^t[\text{N/m}]$	64	Eq. (6)	28	Eq. (6)
			320	[28]

openings, while SB02 contains a $2.26 \times 1.125m^2$ window, horizontally centred and at $0.9m$ from the ground. The walls were tested until failure by applying an incremental uniformly distributed load to their surface with airbags, while only the self-weight acted vertically. The tests were monitored by measuring the internal airbag pressure to quantify the applied load and the horizontal displacement of a control point at the midspan of the top free edge.

The mechanical properties of bricks and mortar are reported in Table 1, where ρ is the material density and the other parameters were previously defined. Only some of them have been experimentally measured by Chong [8], thus, the missing parameters required for the numerical simulations are obtained from the literature. In the following notation, the subscript b refers to "bricks" and m to "mortar", respectively. E_b is assumed equal to $16700MPa$ [29,11].$E_m = 4000MPa$ is determined after numerical investigation of the wall elastic response, consistently with Kaushik et al. [23]. $\sigma_{t,b}$ is considered 10 % of $\sigma_{c,b}$ [14]. $\sigma_{t,m}$ is set equal to $0.58MPa$ following Lourenço [28]. $G_{f,b}^c$ and $G_{f,m}^c$ are taken from Eq. (3). $G_{f,b}^t$ is computed using Eq. (6). Instead, two different literature values are initially considered for $G_{f,m}^t$. One value is obtained from Eq. (6) and one from Lourenço [28] and Pantò et al. [36]. The theoretical calculations (Eq. (6)) show that $G_{f,m}^t$ should be in the range of $28N/m$. Conversely, Lourenço [28], and successively Pantò et al. [36], considered a tenfold value ($320N/m$, obtained by inverse fitting) in replicating the same experiments, which seems unreasonably high for this type of mortar if compared with the data by Pluijm [40] (which aligns with Eq. (6), instead). The results related to these two values are compared later in this section. Finally, ψ_m is set to $43°$ to replicate the shear failure at bed joints under the vertical loads [40], while ψ_b is set to

Table 2
Plasticity input parameter for the CDP.

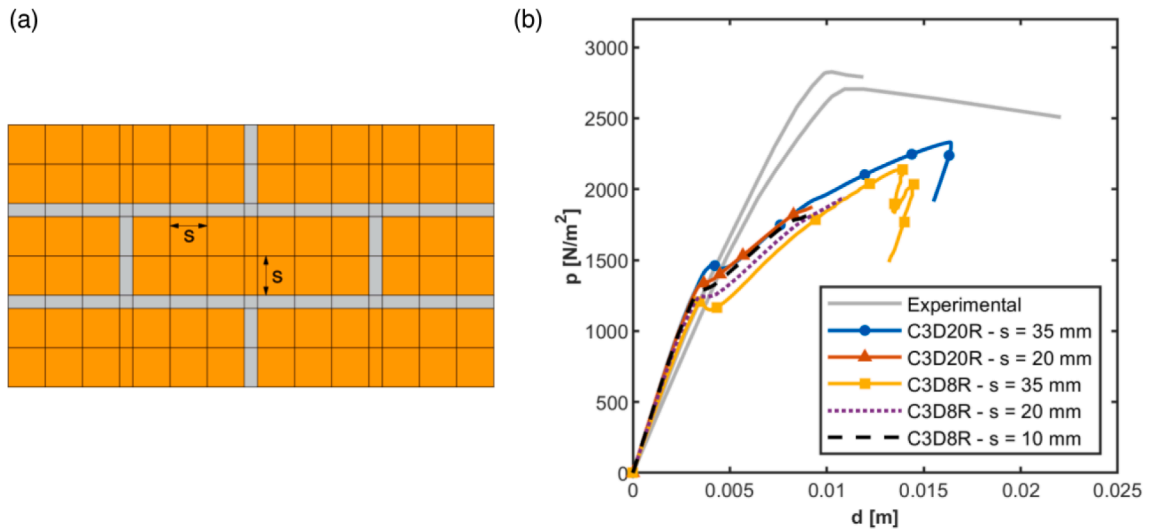| $\psi_m[°]$	$\psi_b[°]$	$\epsilon[-]$	$\sigma_{bo}/\sigma_{c0}[-]$	$K_C[-]$	$\mu[-]$
43	35	0.1	1.16	0.667	0

(a)

(b)

Fig. 3. (a) Wall mesh layout with $s = 35mm$, and (b) mesh sensitivity results for the wall SB01/05.
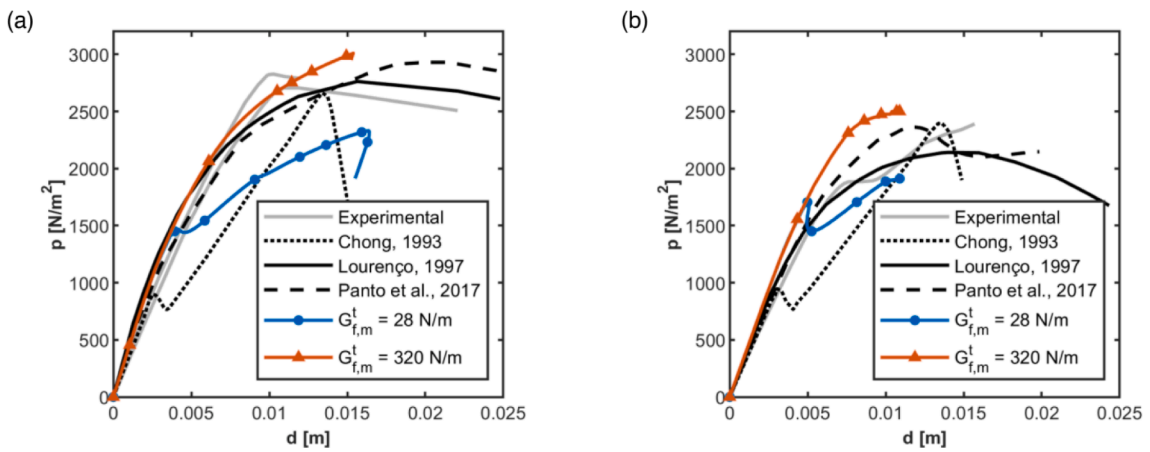
(a)

(b)

Fig. 4. Role of mortar tensile fracture energy on the numerical results: (a) SB01/05 and (b) SB02.
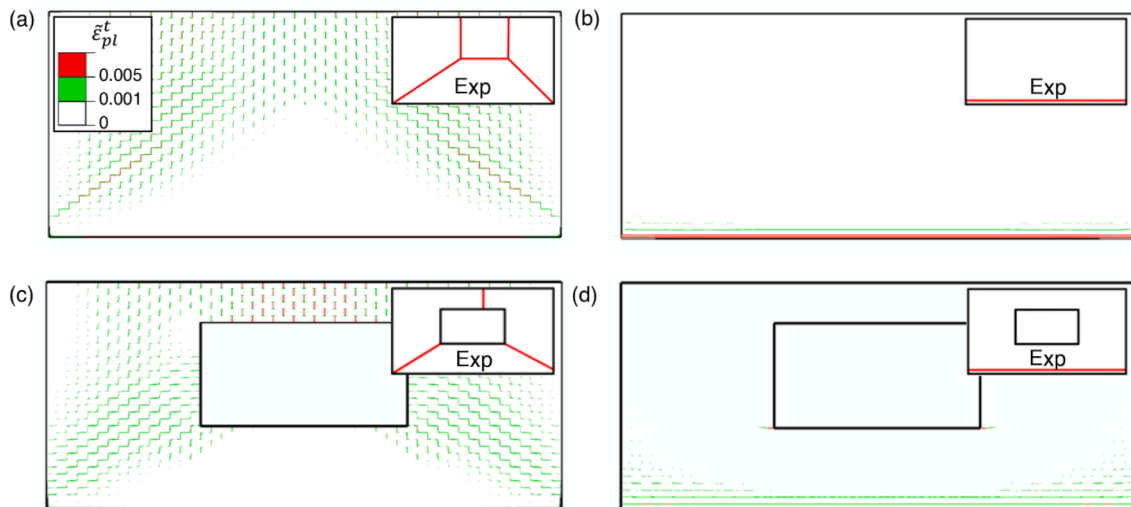
(a)

(b)

(c)

(d)

Fig. 5. Crack patterns at peak load for both the considered $G_{f,m}^t$ (a) SB01/05 – front, (b) SB01/05 – back, (c) SB02 –front and (d) SB02 – back. The thresholds used in the plot contour are set at 30% and 70% post-peak strength loss for mortar. The same values correspond to 60% and 98% of the bricks.
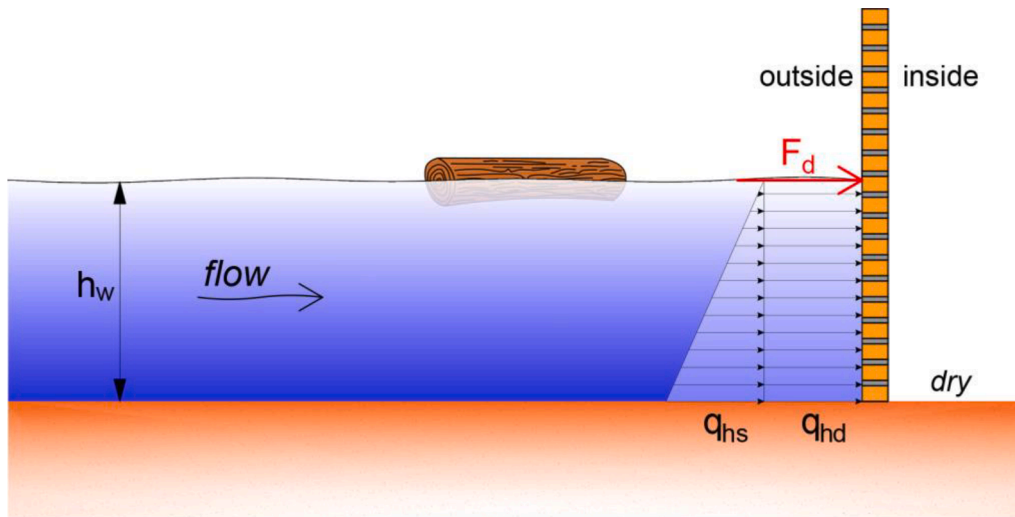
Fig. 6. Vertical section view of the case study.

35° following data from Wosatko et al. [50] for plain concrete without specifics for clay bricks. The default Abaqus values are set for the other CDP input parameters (i.e. ε, σ_{bo}/σ_{c0}, K_c and μ, see Table 2). The analyses are carried out using a Riks' procedure with an implicit solver.

The model is meshed with hexahedral elements. A view of the wall surface shows the mesh layout in Fig. 3-a. The mortar layers contain only one element across their thickness. Aiming at reducing the computational effort by merging the meshes of bricks and mortar, nodes are forced to coincide at the bricks-mortar interfaces. This creates layers of elements across bricks and mortar which have one of the three dimensions fixed by the mortar thickness. Given these constraints, the mesh size is uniquely controlled through the parameter s (see Fig. 3-a). Using $G_{f,m}^t$ from Eq. (6), the mesh sensitivity is investigated on the SB01/05 wall using three mesh sizes ($s = 35$, 20 and $10mm$) together with reduced integration hexahedral linear (C3D8R) and quadratic elements (C3D20R).

The results (Fig. 3-b) show that the wall elastic stiffness related to C3D20R elements is not significantly affected by the mesh size (-0.17% passing from $s = 35mm$ to $s = 20mm$). In contrast, the wall elastic stiffness related to C3D8R elements gradually converges to the quadratic elements results when decreasing the mesh size as, taking as a reference the results using C3D20R with $s = 20mm$, it differs by -11.8%, -3.9% and -1.2% when $s = 35mm$, $20mm$ and $10mm$, respectively. The peak load decreases by 8.1% when using linear elements with respect to quadratic elements in the case of $s = 35mm$. The models with $s = 20$ and $10mm$ aborted before reaching the peak load due to the high computational demand, but the available data are sufficient to judge the mesh sensitivity. Taking as a reference the results using C3D20R with $s = 35mm$ and considering the displacement range of $0.005m$ to $0.01m$, the predicted loads are on average -5.7% and $+0.1\%$ when $s = 20mm$ and C3D8R and C3D20R, respectively, are used. This difference decreases to -1.4% when $s = 10mm$ and C3D8R are used. Overall, it is noted that the general shape of the load–displacement curves and the predicted peak loads are different from the experimental results in all cases. The reason behind such observation is discussed next.

As shown in Fig. 4, using the theoretical value of $G_{f,m}^t$ (i.e. $28N/m$ computed from Eq. (6)) leads to achieving a lower out-of-plane capacity compared to the experiments (-17.5% for SB01 and -20.1% for SB02) but a similar global response to the numerical results of Chong [8] and correct cracking patterns (Fig. 5). Meanwhile, using a higher fracture energy as adapted by other authors (i.e. $320N/m$ from Lourenço [28]) will lead to a good agreement between numerical and experimental results in terms of force–displacement curves using our modelling strategy ($+6.5\%$ for SB01 and $+4.6\%$ for SB02 for the peak load). This

confirms that our numerical model is able to capture a global response that is more aligned with experiments when a very high, but unreasonable, value of $G_{f,m}^t$ is used for mortar as adapted by other authors. It is worth noting, the cracking patterns obtained from $G_{f,m}^t = 320N/m$ are the same as those from the other fracture energy value.

Considering that the aim of this work is to investigate the activation of the high strain rate effects in masonry under debris impact loads, which do not require getting the best fit with the experimental results, but rather to develop a reliable numerical model that can accurately capture the nonlinear response and failure modes of masonry under out-of-plane loads, the authors believe that the selection of reasonable material input parameters (including the value of $G_{f,m}^t$ equal to $28N/m$) is important for drawing reliable conclusions from numerical simulations. However, it is also worth noting that the authors confirmed that the conclusions drawn from the paper do not change if a higher tensile fracture energy is considered for the mortar (see Appendix B).

3. Flow and debris impact loads

The loading scenario is shown in Fig. 6. Two main horizontal loads are applied to the wall surface: the flow actions, which are the hydrostatic (q_{hs}) and hydrodynamic (q_{hd}) pressures, and the debris impact force (F_d). The water depth h_w is assumed to increase gradually until a steady-state condition is reached. Then, the debris impact generates an impulsive load on the wall. A log is selected as one of the most common debris types [15]. The flow and the log are assumed to hit the wall orthogonally, and debris damming is not considered.

3.1. Loads modelling

The hydrostatic pressure on the wall surface has a triangular profile along the water column and is uniform along the width. The value at the bottom is computed using Stevin's formula [9]:

$$q_{hs} = \rho_w g h_w \qquad (14)$$

where ρ_w is the fluid density, g is the gravity acceleration. The structure interior is considered dry, as it is the most critical condition under the hydrostatic pressure [24]. The hydrodynamic component is caused by the water flow, which is considered fully turbulent and in shallow-water conditions [9]. Consequently, the flow velocity profile is modelled as uniform along the water depth and width. It follows that q_{hd} is also uniform along the same directions [24,37,21,3]. The flow is assumed in subcritical condition as it is more relevant to such natural hazards that
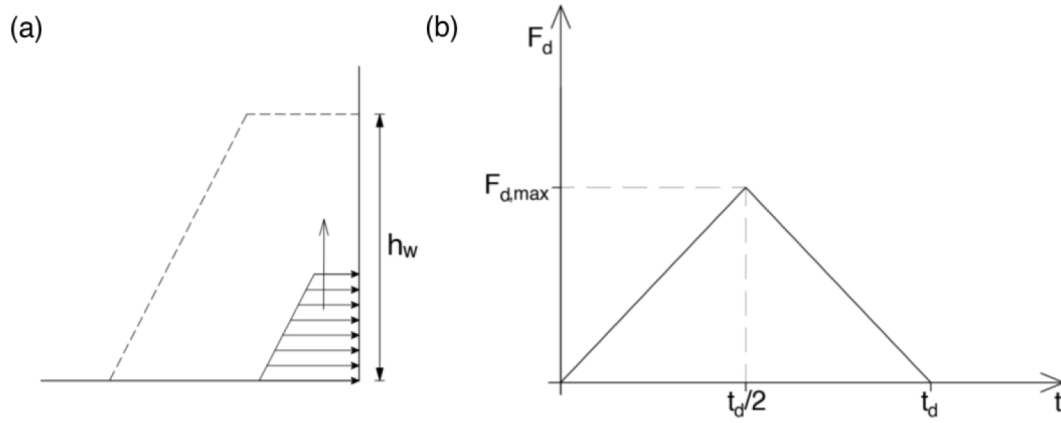
Fig. 7. (a) Flow action evolution during the analysis; (b) Triangular force–time diagram for the debris impact.

can lead to debris transport [37]. Also, as such scenarios are less aggressive, the general belief is that the water-borne debris impacts are less severe in such scenarios, the accuracy of which is under interrogation in the presented paper. It is worth noting that the choice of subcritical conditions is the worst-case scenario for the aim of this study (see Section 1) because it is associated with lower flow velocity than the supercritical condition at the same water depth and, through the lower impact force (see Eq. (19)), with likely lower strain rates (while this study investigates if the induced strain rates are high enough to activate the high strain rate effects). The subcritical condition is adopted in the framework of the shallow water assumption by considering uniform water level along the structure perimeter and ensured by using a Froude number, defined as [42]:

$$Fr = \frac{v_w}{\sqrt{gh_w}} \tag{15}$$

lower than the critical Froud value Fr_c. v_w is the flow velocity, and Fr_c is estimated using the following expressions [42]:

$$\left(1 - \frac{C_H b}{\delta}\right)\frac{1}{2Fr_c^{4/3}} + \left(1 - \frac{C_{hd} b}{2\delta}\right)Fr_c^{2/3} = \left(1 - \frac{C_H b}{\delta}\right)\frac{1}{2Fr_{dc}^{4/3}} + Fr_{dc}^{2/3} \tag{16}$$

$$Fr_{dc} = \left(1 - \frac{C_H b}{\delta}\right)^{1/2} \tag{17}$$

where b is the structure width, δ is the channel width, C_H is experimentally calibrated as 0.58 and Fr_{dc} is the downstream critical Froude number. δ is the relative distance between adjacent buildings for a real hydrodynamic event [41]. A sparse environment is assumed as one of the possible real scenarios, therefore, $\delta \gg b$, $b/\delta \to 0$ and $Fr_c = 1$. Finally, q_{hd} is [42]:

$$q_{hd} = \frac{1}{2}\rho_w C_{hd} v_w^2 \tag{18}$$

where C_{hd} is the drag coefficient, which measures the global resistance a structure opposes to the flow. C_{hd} is, for full buildings, determined from the local pressure coefficients C_p around the structure [21]. Therefore, if

Table 3
Input parameters for loads definition.

Water flow data		Debris data	
h_w[m]	0.9	ρ_d[kg/m³]	690.4
Fr[-]	0.6	φ_d[m]	0.305
b/δ[-]	0	l_d[m]	9
C_p[-]	1.5	E_d[MPa]	7580
ρ_w[kg/m³]	1100	m_d[kg]	454
v_w[m/s]	1.78	k_d[kN/m]	61,300

a single wall is analysed, as in the present case, it is more accurate to replace C_{hd} with the wall C_p to define the hydrodynamic loads [21]. This study uses $C_p = 1.5$ following the experimental data by Jansen et al. [21].

The method prescribed by ASCE/SEI 7-22, based on the contact-stiffness approach [35], is used to determine the debris impact force-–time diagram. This formulation assumes that both the structure and the debris are elastic. The peak force is:

$$F_{d,max} = v_d \sqrt{k_{eff}\, m_d} \tag{19}$$

and the duration is:

$$t_d = \frac{2m_d v_d}{F_{d,max}} = 2\sqrt{\frac{m_d}{k_{eff}}} \tag{20}$$

where v_d is the debris velocity, which is assumed to be equal to v_w, consistently with experimental and numerical findings at the quasi-steady stage of the transport ([34,44,51]; Ruffini et al., 2023), and m_d is the debris mass. k_{eff} is the effective elastic impact stiffness and accounts for the debris-structure interaction. It is computed as [16]:

$$\frac{1}{k_{eff}} = \frac{1}{k_d} + \frac{1}{k_s} \tag{21}$$

where k_d is the debris stiffness and k_s is the structure stiffness. k_d for a log debris is the axial stiffness of a beam-like element and is equal to:

$$k_d = \frac{E_d A_d}{l_d} \tag{22}$$

where E_d is the longitudinal Young's modulus, A_d is the cross-section area, and l_d is the length. Instead, k_s is obtained from preliminary simulations using an arbitrary concentrated force applied along the impact direction. k_s is calculated as the ratio between the force magnitude and the displacement at the application point and parallel to the force. Such a force is implemented as a uniform pressure on an area equal to A_d. Further analyses (not reported here) also showed that this area does not significantly influence k_s (a 2.8% decrease was observed with area diameter reduced by 90%).

The total flow load has a trapezoidal profile (Fig. 7-a) and is applied following the Variable Height Pushover (VHPO) method [37], where the water depth is monotonically increased from zero to h_w while keeping Fr constant (Fig. 7-a). This method simulates the rising water depth during an extreme hydrodynamic event [37]. After the application of the flow action, the debris impact force is applied as a uniform pressure over an area equal to A_d, following a triangular force–time diagram (Fig. 7-b) with a maximum force of $F_{d,max}$ (Eq. (19)), and a duration of t_d (Eq. (20)). Although a rectangular force–time diagram is imposed in ASCE/SEI 7-22 for expressing the debris impact load, recent experimental evidence has
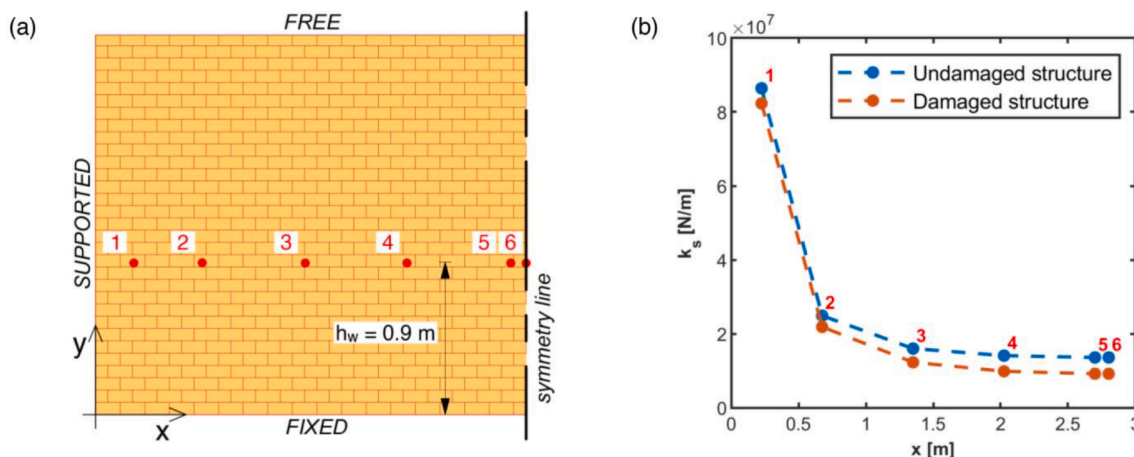
Fig. 8. Structural stiffness (vertical symmetry is exploited): (a) discretised points on the wall and (b) k_s values for the damaged and undamaged structure.

Table 4
Applied actions.

Water flow loads		Debris loads		
			Point 1	Point 6
q_{hs}[MPa]	0.00971	$F_{d,max}$[kN]	227.49	126.67
q_{hd}[MPa]	0.00262	t_d[s]	0.0071	0.0128

shown that a triangular force–time diagram is more accurate for log-type debris [39].

3.2. Loads calculation

h_w is set as $0.9m$, the lowest height at which ASCE/SEI 7-22 considers debris floating. Fr is assumed equal to 0.6 as a possible case of subcritical flow. Once h_w and Fr are fixed, v_w, q_{hs} and q_{hd} are calculated with Eqs. (15), 14 and 18, respectively. $\rho_w = 1100 kg/m^3$ to account for the suspended sediments entrained in the flow [3]. The debris properties are selected according to the minimum demand imposed by ASCE/SEI 7-22 for log-type debris: $m_d = 454kg$ and $k_d = 61300kN/m$, which correspond to a length of $l_d = 9m$, a diameter of $\varphi_d = 0.305m$ and a $E_d = 7550MPa$. $\rho_d = 690.4kg/m^3$ from such data. The loads input parameter are reported in Table 3.

The value of k_s depends on the location of the impact with respect to the boundary conditions. Therefore, different impact points are preliminarily considered (Fig. 8-a). Following the guidelines by ASCE/SEI 7-22, which prescribe that debris impact loads do not need to be combined with other water flow loads, k_s is calculated for the undamaged structure (i.e. not considering the possible stiffness reduction due to damage after the water flow loads application). However, the stiffness of the water-damaged structure is also computed to compare results. Both values are reported in Fig. 8-b. The stiffness reduction of the damaged structure increases going from Point 1 (-9.3%) to Point 6 (-32.4%). As a consequence, if considering the damaged structure, $F_{d,max}$ decreases by 2.1% at Point 1 and by 15.2% at Point 6, while t_d increases by 2.1% at Point 1 and 17.9% at Point 6. Considering such limited variations, and aiming at following ASCE/SEI 7-22 provisions, the undamaged stiffness is used hereafter. However, using the values of the damaged structure would not affect the paper conclusions, as demonstrated in Section 4.4.

Taking as a reference the values at Point 6, the results show that k_s at Points 4, 5 and 6 are similar, as k_s increase only by 1.1% and 4.4% at Points 5 and 4, respectively. Conversely, the increment is higher near the boundaries and equal to 21.2%, 98%, and 610.6% at Points 3, 2 and 1, respectively. As such, Points 1 and 6 are selected for the simulation, and their results are compared. This is expected to cover an acceptable range

of structural stiffnesses and failure modes as bending failure is mainly expected at midspan (i.e. Point 6), while shear failure is likely for impact close to the boundaries (i.e. Point 1). This also aligns with the ASCE/SEI 7-22 recommendations to apply impact loads at positions that maximise bending or shear. The load values are reported in Table 4. Such values also allow to validate the hypothesis of elastic debris made for Eq. (20). Indeed, the maximum impact force considered in this study leads to a peak compressive stress in the debris of $\cong 3$ MPa, which is lower than the typical compressive strength of wood, which ranges between 30 MPa and 50 MPa [22].

4. Debris impact simulations

With the aim of assessing the importance of strain rate effects, the waterborne debris impact on a masonry wall is simulated here following the loading scenario defined in Section 3. The SB01/05 wall, used for validation of the numerical modelling strategy in Section 2.4 with the mechanical properties shown in Table 1, is used for this purpose. No structural damping is introduced as it has little importance in controlling the maximum response of a structure to impulsive loads [10]. Unlike the validation process, where the Abaqus implicit solver was more adequate to replicate the selected experiment, the explicit solution scheme is used here due to its better performance in handling fast-load applications and large element deformations [1]. However, the validation still holds for the explicit solver, as shown in Appendix A. The mesh size, s, is set equal to $35mm$ to minimise the computational effort, and the linear elements (C3D8R) are selected as the only hexahedral element typology allowed by Abaqus explicit [1]. It is worth noting that using C3D8R elements resulted in a lower structural capacity compared to using C3D20R or a smaller mesh size (Fig. 5). However, the mesh sensitivity analysis of the impact simulations shows that $s = 35mm$ is sufficient to reach mesh independency (see Appendix A).

The self-weight of the wall is applied first, followed by the quasi-static application of the flow action, as described in Section 3. The automatically calculated stable time increment Δt_s is used in this phase, which is based on the time a sound wave needs to pass across the element thickness [1]. Then, the impact load is applied following the force–time diagram described in Section 3 and using $\Delta t = 10^{-7}s$, which is selected to be one order of magnitude lower than Δt_s, as recommended by Li [27]. The simulation is stopped when a time equal to $3t_d$ passed after the end of the impact duration.

To investigate if some of the dynamic material properties affect the structural response more than others, DIFs are applied to a different range of properties, considering the following cases:

Table 5
Analysed Gauss points.

Gauss point ID	Position	Stress state	Monitored rate	Notes
GP1	Mortar head joint, close to the impact	Tension	$\dot{\varepsilon}_t$	$\varepsilon_t \gg \varepsilon_c$
GP2	Mortar bed joint, close to the impact	Vertical compression + horizontal shear	$\dot{\varepsilon}_c$	$\varepsilon_t \approx \varepsilon_c$

- DIF applied to the elastic modulus and the tensile and compressive strength and fracture energy, labelled as "DIF(t, c, E(t))" if tensile strain rates are used for calculating the DIF of E, or "DIF(t, c, E(c))" if compressive strain rates are used.
- DIF applied only to the tensile and compressive strength and fracture energy, labelled as "DIF(t, c)".
- DIF applied only to the tensile strength and fracture energy, labelled as "DIF(t)".
- DIF not applied at all, labelled as "NoDIF".
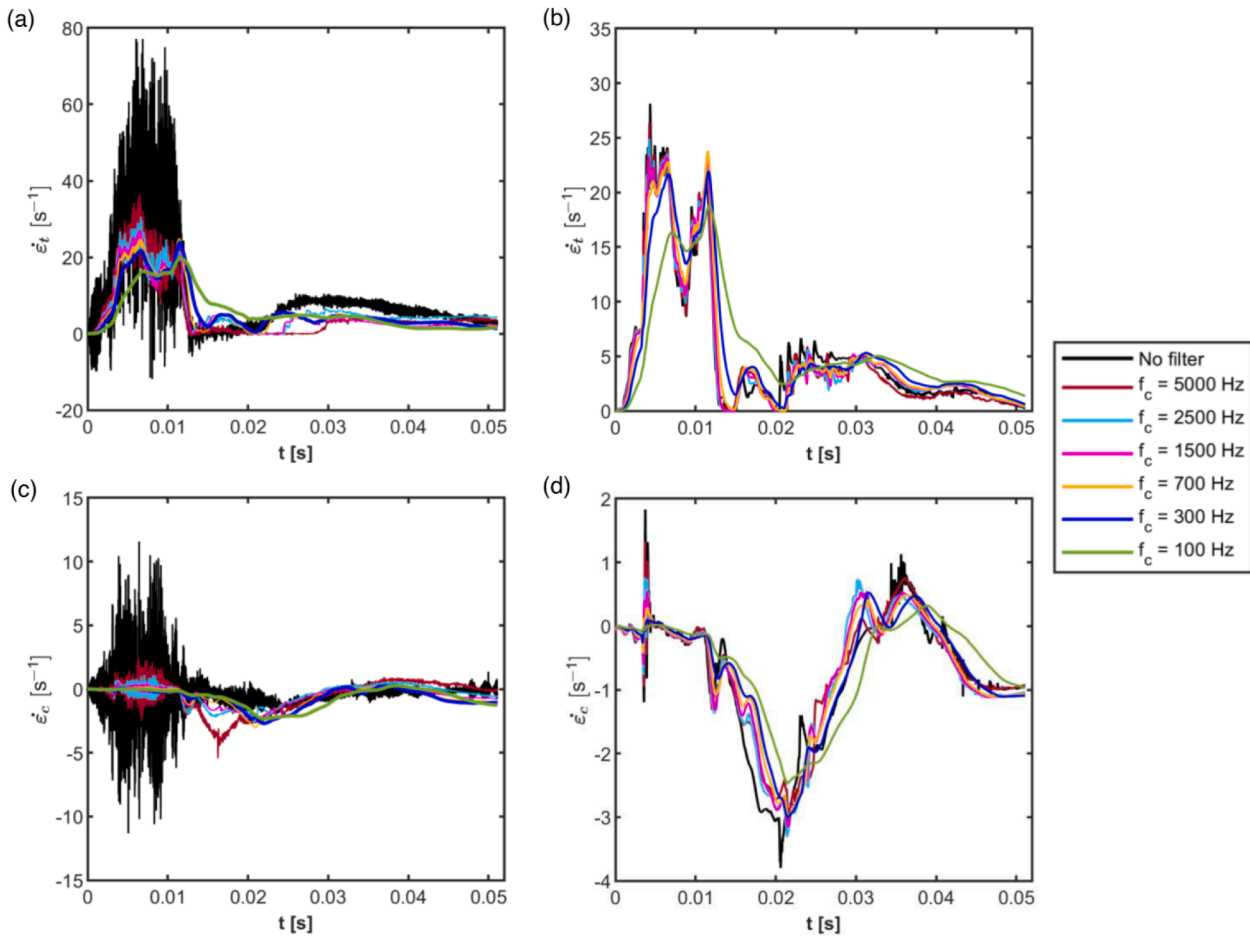
Fig. 9. Strain rate time histories for GP1 using (a) DIF(t, c, E(t)) and (b) DIF(t), and GP2 using (c) DIF(t, c, E(t)) and (d) DIF(t).
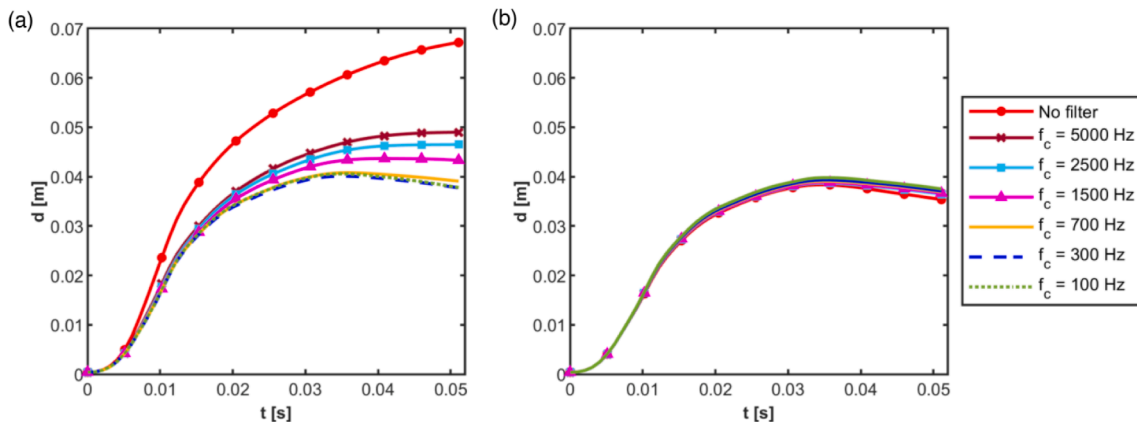

Fig. 10. Horizontal displacement time histories for impacts at Point 6 using different f_c: (a) DIF(t, c, E(t)) cases and (b) DIF(t) cases.
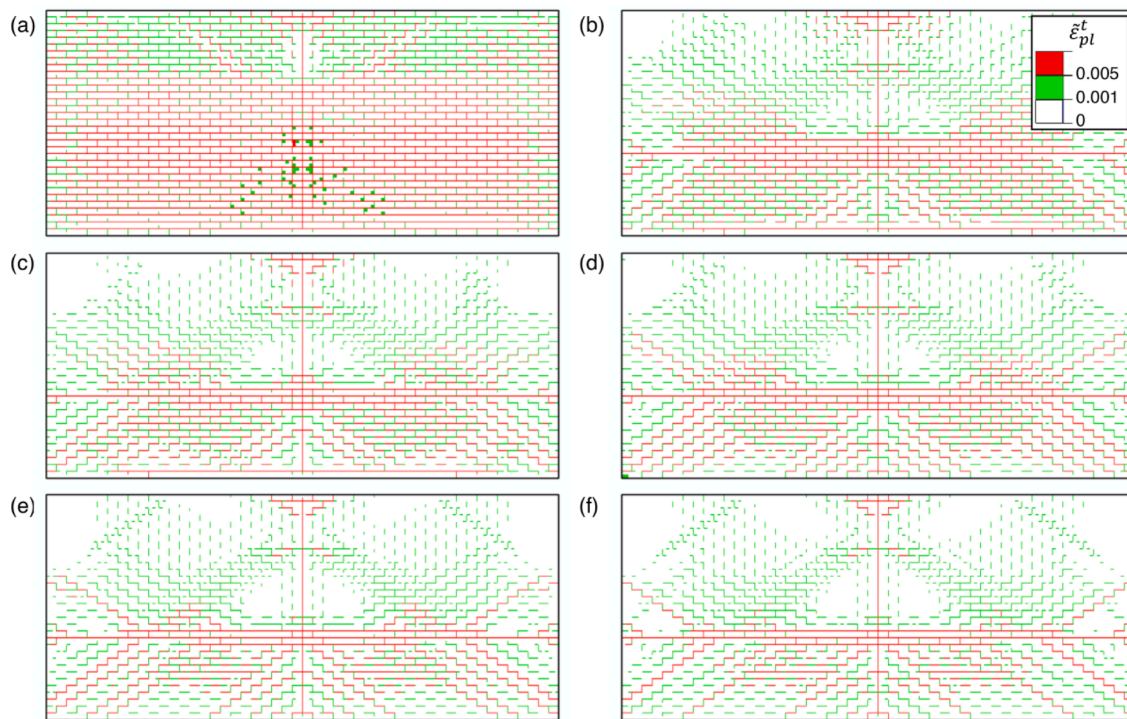
Fig. 11. Crack patterns on the inside face at $t = 4t_d$ using DIF(t, c, E(t)) and (a) no filtering, (b) $f_c = 5000Hz$, (c) $f_c = 300Hz$, (d) $f_c = 100Hz$. Also using (e) DIF(t) with no filtering and (f) DIF(t) with $f_c = 300Hz$.

Table 6
Sensitivity of the results to filtering frequency (f_c).

Case	Strain rates		Displacements		Cracks		Notes
	Level	Effect	Level	Effect	Level	Effect	
DIF(t)	Moderate	Decrease	Low	Increase	No significant variation	None	The maximum displacements slightly increase since the dynamic strength decrease when the strain rates decrease.
DIF(t, c, E(t))	Significant	Decrease	Significant	Decrease	Significant	Decrease	The reduction of the maximum displacements is likely due to removing the high-frequency oscillation effects [27].

4.1. Choice of f_c

As indicated in Section 2.3, the computed strain rates are filtered using Eq. (12), which is a low-pass filter controlled by the smoothing factor ω. The latter is computed from Eq. (13), where the only independent parameter is f_c since Δt is fixed for the impact analyses presented in this study. As the choice of f_c is not established in the literature, it is here investigated how the strain rates are affected by f_c. To do this, their time histories are measured at two different Gauss points (GP), GP1 and GP2 (Table 5), representing a tensile and a compression-shear failure mode to monitor the tensile and compressive strain rates. The sensitivity of the structural displacements and crack patterns is also investigated. The baseline outputs are those related to the nonfiltered simulations.

To select the range of f_c to use in the sensitivity analysis, the power spectra of the non-filtered rate signal are analysed. These outputs indicate that the most powerful frequencies are lower than 150Hz, which likely are the physical oscillations. For higher frequencies, data clearly show a low power noise, with some peaks between 2500Hz and 4500Hz, which could be due to non-physical oscillations, but this cannot be confirmed. Considering this information, the selected f_c for the sensitivity analysis are 100Hz, 300Hz, 700Hz, 1500Hz, 2500Hz and 5000Hz.

In the DIF(t, c, E(t)) cases, the maximum tensile and compressive are reduced, respectively, by 74.1% and 98.1% in the monitored Gauss points when $f_c = 100Hz$ (Fig. 9 - a and c). Moreover, the maximum

displacement of the control point is reduced by 40.3% when $f_c = 100Hz$ (Fig. 10 – a). The crack patterns have also visibly changed as f_c is decreased (Fig. 11 - a to d). Conversely, in the DIF(t) cases, the sensitivity is generally lower. Indeed, the maximum tensile and compressive are reduced, respectively, by 33.1% and 82.7% (Fig. 9 - b, d), and the maximum displacement at the control point is increased by 3.7% when $f_c = 100Hz$ (Fig. 10 - b). The crack patterns are also not visibly changing with decrement of f_c (Fig. 11 - e, f). The discussion made for DIF(t, c, E(t)) and DIF(t) holds also for the DIF(t, c, E(c)) and DIF(t, c) cases, respectively. These observations are summarised in Table 6 for different DIF cases.

The results shown here support the hypothesis that the sensitivity to f_c is high only when the DIF of the material Young's moduli are included, likely because the strain rates signal contains much more oscillations in these cases (see Fig. 9). Such oscillations might be due to the changes in the global stiffness matrix caused by the rate-dependent Young's moduli. The high strain rate oscillations are causing much higher displacements and damage, consistently with the observation made by Li [27]. More general guidelines on the selection of f_c require further in-depth studies. However, as the sensitivity of the results to f_c diminishes for $f_c \cong 300$ (see Fig. 9, Fig. 10 and Fig. 11), this value is chosen hereafter. Such frequency corresponds to $\omega = 0.000109$ from Eq. (13), which is in agreement with Li [27], in which $\omega = 0.000102$, with $f_c = 200Hz$ and $\Delta t = 1.4\ 10^{-7}s$.
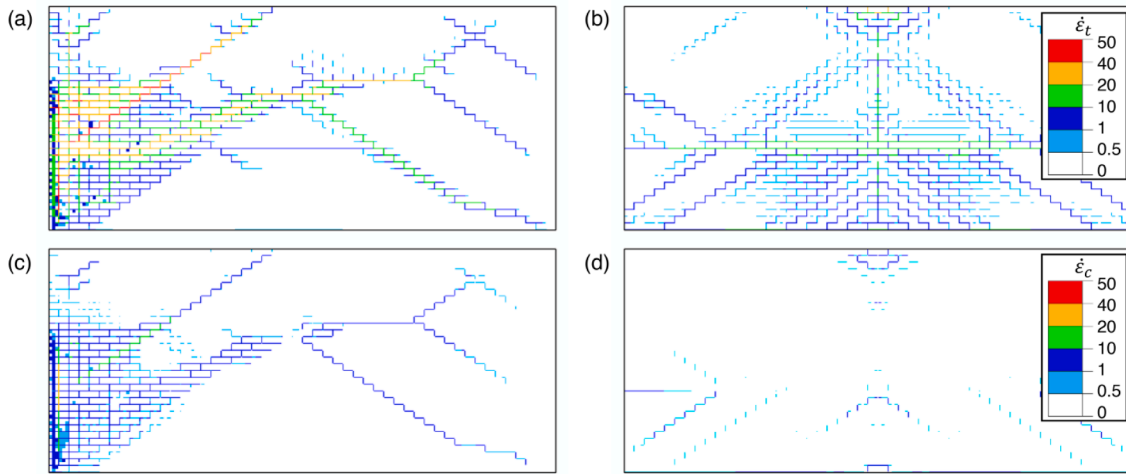
Fig. 12. Envelope of the maximum strain rates on the inside wall face (see Fig. 6): (a) $\dot{\varepsilon}_t$ and (c) $\dot{\varepsilon}_c$ for impact at Point 1, and (b) $\dot{\varepsilon}_t$ and (d) $\dot{\varepsilon}_c$ for impact at Point 6.
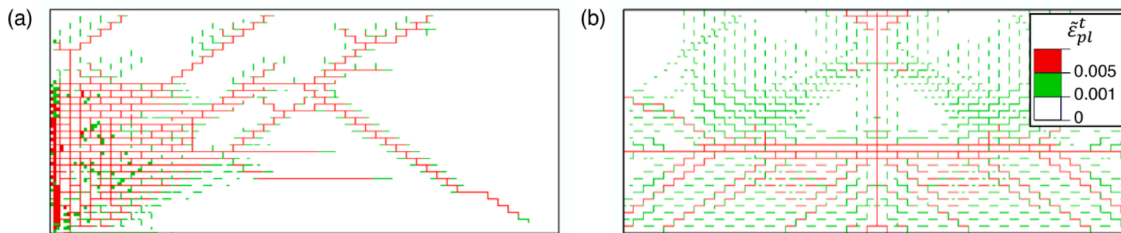

Fig. 13. Crack patterns for impacts at (a) Point 6 in cases (a) NoDIF and (b) DIF(t), and at Point 1 in cases (c) NoDIF and (d) DIF(t).
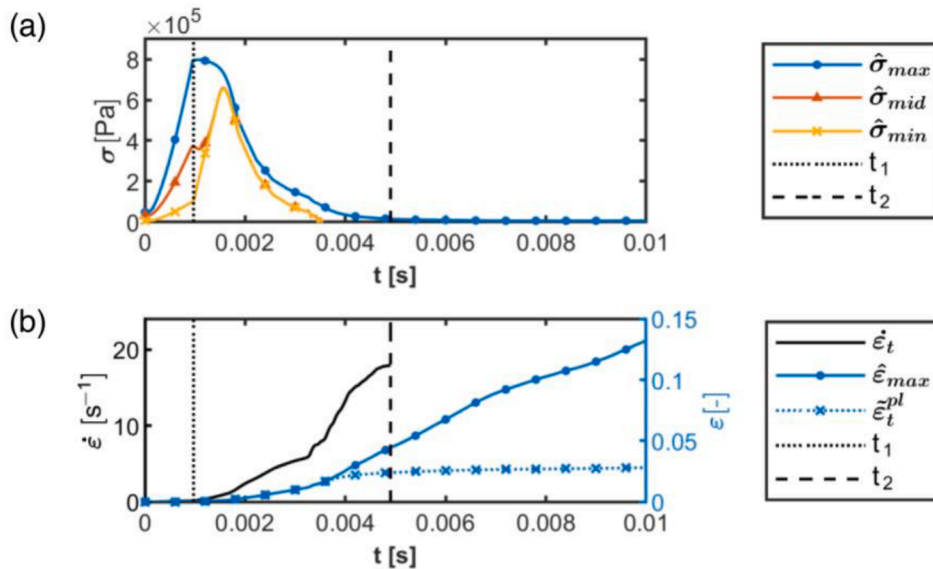

Fig. 14. Evolution of stresses, strains and strain rates component at GP1 for impacts at Point 6.

4.2. Activation of the strain rate effects

The maximum strain rates in tension and compression computed at the studied wall are presented in this section. To understand the importance of the wall out-of-plane stiffness and the induced internal actions (i.e. bending and shear), two cases of debris impact are considered: one impact at Point 6 and one at Point 1.

The envelopes of the maximum strain rates are presented in Fig. 12. In the case where the impact occurs at Point 1, the maximum tensile

strain rate, $\dot{\varepsilon}_t$, is $50s^{-1}$ (Fig. 12-a), while the maximum compressive strain rate, $\dot{\varepsilon}_c$, is $49s^{-1}$ (Fig. 12-c). The corresponding $\dot{\varepsilon}_t$ and $\dot{\varepsilon}_c$ for the impact at Point 6 are $50s^{-1}$ and $49s^{-1}$, respectively (Fig. 12-b,d). These results demonstrate that the strain rate effects are activated in such scenarios as the strain rate values exceed the critical threshold (identified in Section 2.3) over which strain rate effects are considerable. It is worth noting that $\dot{\varepsilon}_t$ and $\dot{\varepsilon}_c$ are two times and five times higher, respectively, for impact at Point 1 compared to impact at Point 6. Moreover, the maximum $\dot{\varepsilon}_c$ for impact at Point 6 are localised on a
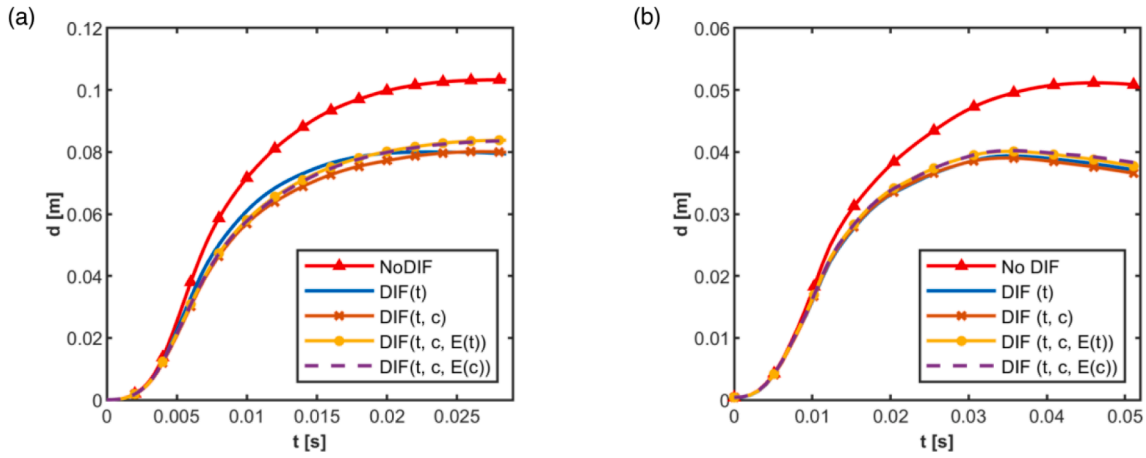
Fig. 15. Horizontal displacement time histories for impacts at (a) Point 1 and (b) Point 6. The control point is the impact one.

smaller area than Point 1. Such results highlight that the impact location along the wall affects the strain rate values. This is because of the differences in the structural stiffness and activated failure modes when the impact occurs at these two locations. The higher stiffness at Point 1, which determines higher peak force and shorter impact time (see Section 3), causes higher strain rates. Furthermore, the crack patterns (Fig. 13) help better understand why the compressive rate values are different between Points 1 and 6. Indeed, impact at Point 6 mainly causes bending cracks in the wall, where tensile stresses and strains are primarily active. Conversely, impact at Point 1 also causes shear cracks, along which significant compressive stresses and strains (and, consequently, strain rates) develop.

Finally, the evolution of stresses, strains and strain rates at GP1 (see Table 5) is shown in Fig. 14 as an example. Here, $\hat{\sigma}_{max}$, $\hat{\sigma}_{mid}$ and $\hat{\sigma}_{min}$ are the maximum, intermediate and minimum principal stresses, the time t_1 is the moment at which the material enters the post-elastic phase, and t_2 is when the material is failed (see Section 2.3). The other parameters present in Fig. 14 were previously defined (see Section 2). It can be observed that the GP1 is under a triaxial tensile stress state and enters the post-elastic phase at t_1, where it reaches a peak $\hat{\sigma}_{max}$ equal to $0.79MPa$ (Fig. 14 - a). The deformation process is visible in Fig. 14 - b, where $\hat{\varepsilon}_{max}$ is monotonically increasing, and $\tilde{\varepsilon}_{pl}$ is approaching its maximum at t_2, confirming the material failure. In this framework, $\dot{\varepsilon}_t$ is small before t_1 (where it is equal to $0.1s^{-1}$), and it grows rapidly between t_1 and t_2, reaching a maximum of $18.2s^{-1}$. After t_2, $\dot{\varepsilon}_t$ is fixed as zero (see Section 2.3). The maximum achieved $\hat{\sigma}_{max}$ confirms that the high strain

rate effects are active as the static tensile strength is $0.58MPa$ (see Table 1). It is also interesting to note that the low strain rates recorded at $t = t_1$ (end of the elastic stage) correspond to a small DIF for E_m (Eq. (8)) and almost a DIF of 1.0 for E_b (Eq. (10)). Therefore, the dynamic enhancement of the materials stiffness is very low in the studied cases.

4.3. Most influential dynamic material properties

The importance of different dynamic material properties is presented in this section by analysing the displacement time histories and the crack patterns. The time histories of the horizontal displacements d of the walls for impact at Points 1 and 6 are shown in Fig. 15. The results show that the maximum displacement d_{max} is 20% less than that of the NoDIF case, independently from the impact location and the DIF cases used. Moreover, the different DIF cases give similar outputs. Comparing the results for cases with DIF(t) and DIF(t, c), it is noted that results are similar for impact at Point 6, and the cases with DIF(t, c) show only a slightly lower d (5% maximum) than the cases with DIF(t) for the impact at Point 1. Similarly, passing from DIF(t, c) to DIF(t, c, E(t)) or DIF(t, c, E(c)), d_{max} increases 1% for the impact at Point 6 and 5% at Point 1.

These findings highlight that the dynamic tensile post-elastic behaviour of the materials is the most influencing dynamic material behaviour that affects the structural response of the studied wall. On the other hand, the importance of the dynamic compressive post-elastic behaviour is correlated with the impact location, in line with what has
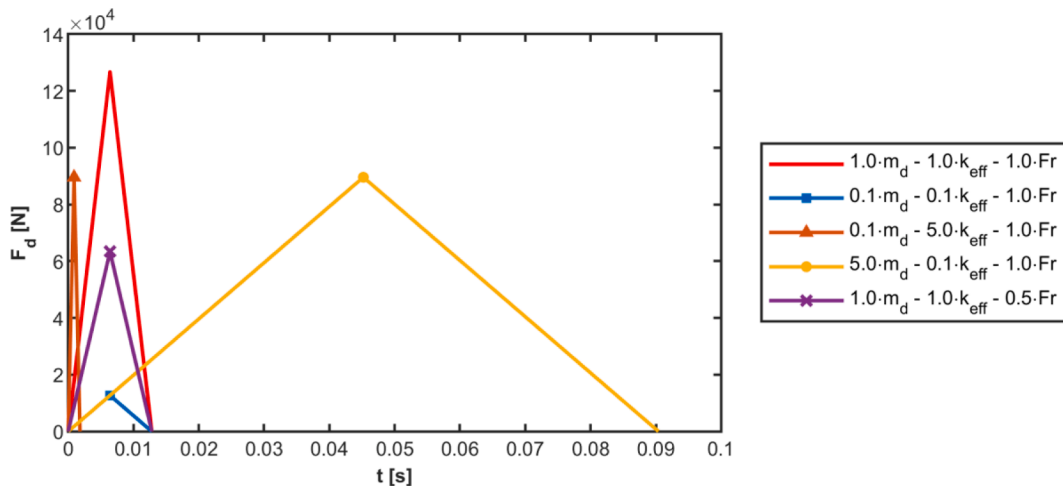

Fig. 16. Force-time diagrams used for the sensitivity analysis on the importance of the strain rate.

Table 7

Outputs for different force–time diagrams.

Case	Variation of $F_{d,max}$	Variation of t_d	Maximum $\dot{\varepsilon}_t$ at GP1	Maximum $\dot{\varepsilon}_c$ at GP2	Reduction of d_{max} from the NoDIF case.
1.0 m_d– 1.0 k_{eff}	–	–	22	3.9	20%
1.0 *Fr*					
0.1 m_d– 0.1 k_{eff}	−90%	0%	0.15	0.025	2.5%
1.0 *Fr*					
0.1 m_d– 5.0 k_{eff}	−29.3%	−85.9%	8.4	0.31	14%
1.0 *Fr*					
5.0 m_d– 0.1 k_{eff}	−29.3%	+ 607.1%	25	2	8%
1.0 *Fr*					
1.0 m_d– 1.0 k_{eff}	−50%	0%	12	0.15	19%
0.5 *Fr*					

been reported in Section 4.2. There, it was pointed out that the significant shear cracks that arise for the impact at Point 1 cause compressive strain rates significantly higher than those at Point 6. In light of the displacement results presented in this section, it is possible that, notwithstanding the compressive strain rate exceeded the critical threshold also for the impact at Point 6 (see Section 4.2), the limited area covered by the maximum compressive rates in such case (see Fig. 12) is not sufficient to modify the structural response (Fig. 15-b). Conversely, the bigger extension of the high compressive rate zone observed for impact at Point 1 (see Section 4.2), together with higher compressive strain rates, modifies the structural response (Fig. 15-a). Finally, the small variations in the displacements time histories when using the strain rate dependent Young's modulus (Fig. 15) confirms the observation made in Section 4.2 about the low importance of the dynamic elastic behaviour, although the influence of f_c on the results should also be carefully considered for drawing any conclusions. To support this finding, it is also worth comparing the maximum strain rate maps (Fig. 12) with the crack patterns (Fig. 13) and noting that maxima and minima strain rates develop along the main cracks, which confirms the strain rate effects are significant mainly where the materials are in the post-elastic phase.

4.4. Activation of the strain rate effects for different force–time diagrams

In the previous sections, it is shown that significant strain rates were developed in the studied masonry walls under the impact of a debris with minimum mass and stiffness proposed by ASCE/SEI 7-22. To evaluate the applicability of the conclusions of the present study to a broader range of debris impact scenarios, further numerical simulations are conducted considering a set of less severe force–time diagrams. The additional force–time diagrams are defined using a wider range of debris typologies by varying k_d and m_d, or flow regimes, by varying *Fr* to obtain a lower peak force or higher impact duration. The impact loads are applied at Point 6 (see Fig. 8-a). It should also be noted that these values are chosen to investigate the extreme debris and mass combination scenarios and do not necessarily correspond to realistic debris typologies.

The changes in the v_w, k_d (and consequently k_{eff}) and m_d lead to changes in the force–time debris impact diagrams as shown in Fig. 16. The key variation of the force–time diagram parameters and the findings of these simulations are reported in Table 7. It is observed that the maximum strain rates depend on the applied load, and their values are lower than in simulations presented in Section 4.2, but still exceed the strain rate effects threshold. Moreover, the difference in the displacement with respect to the NoDIF case is not negligible as it is for the results presented before (see Section 4.3). These results show that the activation of the strain rate effects is not limited to the minimum debris properties suggested by ASCE, but it also holds for a broader range of

debris impact scenarios, i.e. different boundary conditions, materials properties, impact location and flow velocity. Such a finding also demonstrated that the force–time diagram obtained from the reduction of the structural stiffness due to structural damage before the impact does not affect the conclusions of this study.

5. Conclusions

A numerical investigation was presented in this study to understand if high strain rate effects (i.e. the strain rate dependency of the material properties) are activated when analysing the response of masonry structures to waterborne debris impact. The impact load was considered to occur during an extreme hydrodynamic event compatible with shallow-water flow conditions and following the recommendations of ASCE/SEI 7-22. Nonlinear FE simulations were carried out by modelling a masonry wall following a micro-modelling approach (used for the first time in this field) and applying the flow actions and debris impact loads as equivalent forces. To account for the strain rate effects, the strain rate dependent material properties were included in the model using a set of experimental Dynamic Incremental Factors (DIF) taken from the literature. A cut-off frequency f_c was applied to the strain rate signals to remove the oscillations associated with numerical solutions. After having carried out a series of sensitivity analyses on its value, $f_c = 300Hz$ was selected as a reasonable choice for this work because this was the value for which the results sensitivity sensibility slowed down, and that reduced the high damage, also observed by Li [27], caused by poor filtering. The need for further investigations in this area was also highlighted, but the conclusion of this paper would not change if a higher f_c have been chosen as the maximum strain rates increase as f_c increases (see Fig. 9). Moreover, the chosen f_c determines a similar smoothing factor ω to Li [27] (see Section 4.1). The main conclusions of this paper are as follows:

1. The strain rate effects were activated in the studied scenarios as the tensile and compressive strain rates were higher than the critical thresholds above which the strain rate effects are usually considered significant. This opens a new research area in this field and presents a critique of the accuracy of previous efforts in numerical simulation or experimental characterisation of such scenarios. This finding, initially obtained using the minimum design demand for log-type debris imposed by ASCE/SEI 7-22, was further extended to a range of impact force–time diagrams different in impact duration and peak force (corresponding to different debris properties or flow velocities). It was also found that the maximum rates depend on the impact location along the wall. This was because of the differences in the structural stiffness and activated failure modes. Higher values of structural stiffness at the impact location were associated with generally higher rates. Instead, different failure modes induced
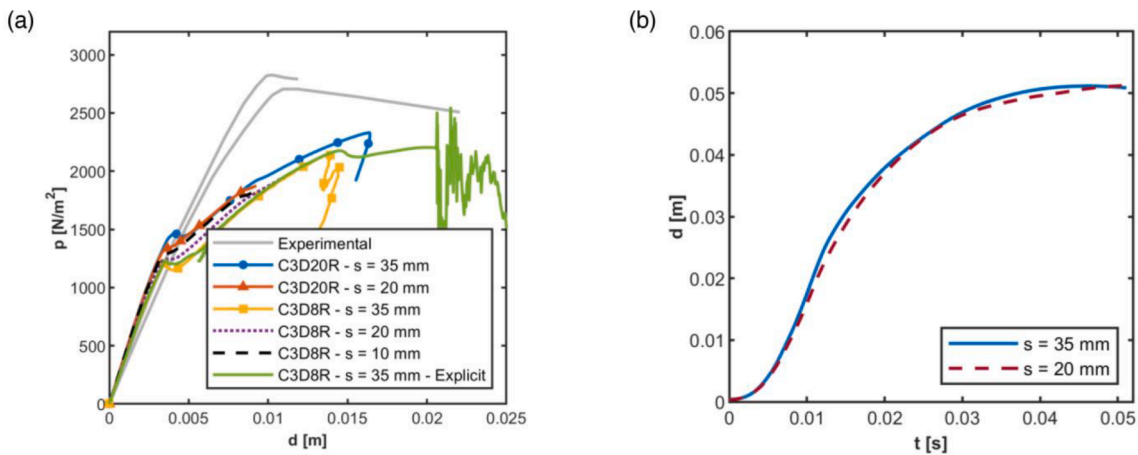
Fig. A1. (a) Validation of the explicit solver results. (b) Mesh sensitivity for the impact analyses using the explicit solver.
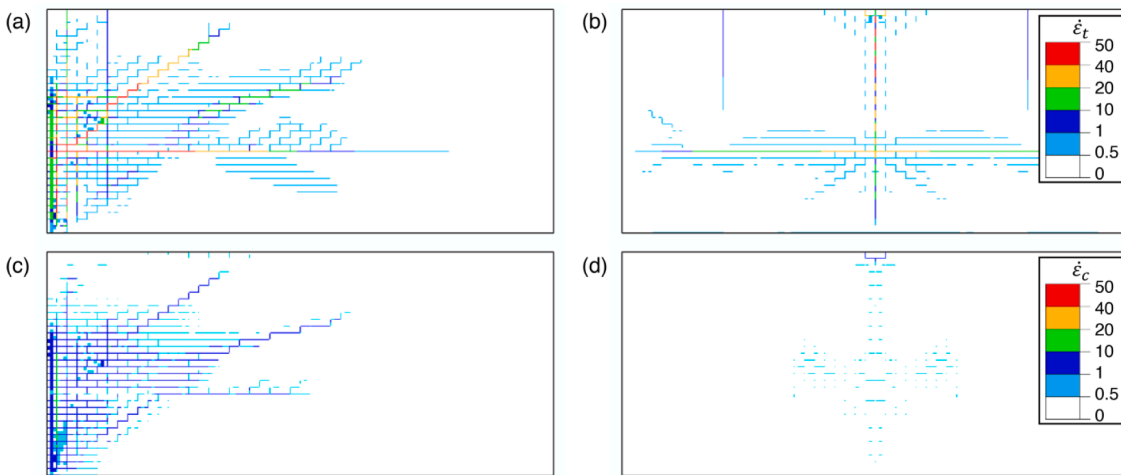

Fig. B1. Envelope of the maximum strain rates on the inside wall face (see Fig. 6) using $G_{f,m}^t = 320N/m$: (a) $\dot{\varepsilon}_t$ and (c) $\dot{\varepsilon}_c$ for impact at Point 1, and (b) $\dot{\varepsilon}_t$ and (d) $\dot{\varepsilon}_c$ for impact at Point 6.

different maximum values of tensile and compressive rates because bending cracks mainly caused high tensile strain rates, while shear cracks caused both high tensile and compressive strain rates. These findings show that a reliable evaluation of the structural response requires considering the currently neglected effect of high strain rate effects in materials constitutive laws. Moreover, they indicate the need for consideration of the debris impact at a number of critical locations along walls at the design or assessment stages.

2. By comparing the displacement time histories, the dynamic tensile post-elastic behaviour of bricks and mortar was found to be the most influencing dynamic material behaviour that affects the structural response, as the differences between the simulations that included the DIF on the tensile post-elastic behaviours only and those that implemented the DIF on both tensile and compressive post-elastic behaviours and the elastic material stiffness were limited (5% difference at maximum). The compressive post-elastic behaviour was found to be more significant when the compressive-shear failure mechanism was activated (i.e. for impacts close to the vertical boundary). Finally, the dynamic elastic behaviour was found to be irrelevant as the strain rates only became sufficiently high in the post-elastic phase of the response. This conclusion can guide future design of experiments (not only in water-borne debris impact scenarios, but also in other studies that involve high strain rate out-of-plane loading on masonry) to ensure that relevant and sufficient data are captured for reliable numerical simulations.

The results presented in this study are a first step towards understanding the response of masonry to waterborne debris impacts. Hence there is a need for future investigations in this field. An important limitation of the present study is the assumption of elastic structure when calculating the impact force. As the inelastic behaviour of the debris decreases the peak force and increases the impact duration [38], the structure nonlinearities may have similar effects, but this has never been investigated before. This represents a potentially valuable future research topic to improve numerical methods to simulate waterborne debris impacts on masonry structures.

CRediT authorship contribution statement

Alessandro De Iasio: Conceptualization, Methodology, Software, Validation, Formal analysis, Investigation, Resources, Visualization, Data curation, Writing – original draft, Writing – review & editing, Visualization. **Bahman Ghiassi:** Conceptualization, Methodology, Formal analysis, Writing – original draft, Writing – review & editing, Supervision, Project administration, Funding acquisition. **Riccardo Briganti:** Conceptualization, Methodology, Formal analysis, Writing – original draft, Writing – review & editing, Supervision, Project administration. **Gabriele Milani:** Conceptualization, Methodology, Writing – review & editing.

Declaration of Competing Interest

The authors declare that they have no known competing financial interests or personal relationships that could have appeared to influence the work reported in this paper.

Data availability

Data will be made available on request.

Acknowledgements

Appendix A

The validity of the explicit solver to simulate the experimental results shown in Section 2.4 is proved in Fig. A1 - a. The mesh sensitivity of the impact analysis is negligible since the increase of the maximum displacement is 0.13% when using $s = 20mm$ (Fig. A1 - b).

Appendix B

Fig. B1 demonstrates that the strain rate effects are activated in the studied scenarios also if $G^t_{f,m} = 320N/m$ is used in the simulations as the strain rate values exceed the critical threshold (identified in Section 2.3) over which strain rate effects are considerable. Therefore, the main conclusions drawn from the paper do not change if a higher value of $G^t_{f,m}$ is considered.

References

[1] Abaqus, 2018. Abaqus User Manual. Dassault Systèmes Simulia Corp, United States.

[2] Alfarah B, López-Almansa F, Oller S. New methodology for calculating damage variables evolution in Plastic Damage Model for RC structures. Eng Struct 2017; 132:70–86. https://doi.org/10.1016/j.engstruct.2016.11.022.

[3] ASCE, 2022. Minimum Design Loads and Associated Criteria for Buildings and Other Structures. ASCE/SEI 7-22. Reston, VA.

[4] Ayhan B, Lale E. Modeling strain rate effect on tensile strength of concrete using damage plasticity model. Int J Impact Eng 2022;162. https://doi.org/10.1016/j.ijimpeng.2021.104132.

[5] Bažant ZP, Oh BH. Crack band theory for fracture of concrete. Mat Constr 1983;16 (3):155–77.

[6] Cahuzac, A., Boudet, J., Borgnat, P., Lévêque, E., 2010. Smoothing algorithms for mean-flow extraction in large-eddy simulation of complex turbulent flows. Physics of Fluids 22, 125104. https://doi.org/10.1063/1.3490063.

[7] Cavaleri L, Ciraolo G, Ferrotto MF, La Loggia G, Lo Re C, Manno G. Masonry structures subjected to tsunami loads: Modeling issues and application to a case study. Structures 2020;27:2192–207.

[8] Chong VL. The behaviour of laterally loaded masonry panels with openings (PhD Thesis). University of Plymouth, Plymouth; 1993.

[9] Te Chow V. Open-channel hydraulics. McGraw-Hill, New York: McGraw-Hill civil engineering series; 1959.

[10] Clough RW, Penzien J. Dynamics of structures. 2nd ed. New York: McGraw-Hill; 1993.

[11] D'Altri AM, de Miranda S, Castellazzi G, Sarhosis V. A 3D detailed micro-model for the in-plane and out-of-plane numerical analysis of masonry panels. Comput Struct 2018;206:18–30. https://doi.org/10.1016/j.compstruc.2018.06.007.

[12] Drougkas A, Roca P, Molins C. Numerical prediction of the behavior, strength and elasticity of masonry in compression. Eng Struct 2015;90:15–28. https://doi.org/10.1016/j.engstruct.2015.02.011.

[13] Feenstra PH. Computational Aspects of Biaxial Stress in Plain and Reinforced Concrete (PhD dissertation). Delft University of Technology, Delft, The Netherlands; 1993.

[14] Ghiassi B, Milani G. Numerical modelling of masonry and historical structures: From theory to application. Numer Model Masonry Historical Struct: From Theory Appl 2019;1–795. https://doi.org/10.1016/C2017-0-01579-3.

[15] Haehnel R, Daly S. Debris impact tests. Report for the American Society of Civil Engineers by the U.S. Army Cold Regions Research and Engineering Laboratory. Hanover, NH; 2001.

[16] Haehnel RB, Daly SF. Maximum Impact Force of Woody Debris on Floodplain Structures. J Hydraul Eng 2004;130:112–20. https://doi.org/10.1061/(ASCE)0733-9429(2004)130:2(112).

[17] Hao H, Tarasov BG. Experimental Study of Dynamic Material Properties of Clay Brick and Mortar at Different Strain Rates. Aust J Struct Eng 2008;8(2):117–32.

[18] Hordijk DA. Local approach to fracture of concrete. Delft University of Technology, Delft, The Netherlands; 1991.

[19] Jalayer F, Aronica GT, Recupero A, Carozza S, Manfredi G. Debris flow damage incurred to buildings: an in situ back analysis. J Flood Risk Manag 2018;11. https://doi.org/10.1111/jfr3.12238. S646–S662.

[20] Jalayer F, Carozza S, de Risi R, Manfredi G, Mbuya E. Performance-based flood safety-checking for non-engineered masonry structures. Eng Struct 2016;106: 109–23. https://doi.org/10.1016/j.engstruct.2015.10.007.

[21] Jansen L, Korswagen PA, Bricker JD, Pasterkamp S, de Bruijn KM, Jonkman SN. Experimental determination of pressure coefficients for flood loading of walls of Dutch terraced houses. Eng Struct 2020;216:110647.

[22] Kasal B. Wood formation and properties. Mechanical Properties of Wood. Encyclopedia For Sci. 2004;1815–1828. https://doi.org/10.1016/B0-12-145160-7/00041-7.

[23] Kaushik HB, Rai DC, Jain SK. Stress-Strain Characteristics of Clay Brick Masonry under Uniaxial Compression. J Mater Civ Eng 2007;19(9):728–39.

[24] Kelman I, Spence R. A limit analysis of unreinforced masonry failing under flood water pressures. Masonry Int J Brit Masonry Soc 2003;16.

[25] Korswagen P, Selvam H, Oetjen J, Wüthrich D. Post-flood field survey of the Ahr Valley (Germany) - Building damages and hydraulic aspects; 2022.

[26] Lee J, Fenves GL. Plastic-Damage Model for Cyclic Loading of Concrete Structures. J Eng Mech 1998;124:892–900. https://doi.org/10.1061/(ASCE)0733-9399(1998)124:8(892).

[27] Li X.X. (Lambert). Parametric study on numerical simulation of missile punching test using concrete damaged plasticity (CDP) model. Int J Impact Eng 2020;144: 103652. https://doi.org/10.1016/J.IJIMPENG.2020.103652.

[28] Lourenço PB. An anisotropic macro-model for masonry plates and shells: implementation and validation; 1997.

[29] Lourenço PJBB. Computational strategies for masonry structures. Delft University of Technology; 1996.

[30] Lubliner J, Oliver J, Oller S, Oñate E. A plastic-damage model for concrete. Int J Solids Struct 1989;25:299–326. https://doi.org/10.1016/0020-7683(89)90050-4.

[31] Majtan E, Cunningham LS, Rogers BD. Numerical study on the structural response of a masonry arch bridge subject to flood flow and debris impact. Structures 2023; 48:782–97. https://doi.org/10.1016/j.istruc.2022.12.100.

[32] Majtan E, Cunningham LS, Rogers BD. Flood-Induced Hydrodynamic and Debris Impact Forces on Single-Span Masonry Arch Bridge. J Hydraul Eng 2021;147. https://doi.org/10.1061/(asce)hy.1943-7900.0001932.

[33] Milanesi L, Pilotti M, Belleri A, Marini A, Fuchs S. Vulnerability to Flash Floods: A Simplified Structural Model for Masonry Buildings. Water Resour Res 2018;54: 7177–97. https://doi.org/10.1029/2018WR022577.

[34] Nistor I, Goseberg N, Stolle J. Tsunami-driven debris motion and loads: A critical review. Front Built Environ 2017;3. https://doi.org/10.3389/fbuil.2017.00002.

[35] Paczkowski K, Riggs HR, Naito CJ, Lehmann A. A one-dimensional model for impact forces resulting from high mass, low velocity debris. Struct Eng Mech 2012; 42:831–47. https://doi.org/10.12989/SEM.2012.42.6.831.

[36] Pantò B, Cannizzaro F, Caliò I, Lourenço PB. Numerical and Experimental Validation of a 3D Macro-Model for the In-Plane and Out-Of-Plane Behavior of Unreinforced Masonry Walls. Int J Arch Heritage 2017;11:946–64. https://doi.org/10.1080/15583058.2017.1325539.

[37] Petrone C, Rossetto T, Goda K. Fragility assessment of a RC structure under tsunami actions via nonlinear static and dynamic analyses. Eng Struct 2017;136:36–53. https://doi.org/10.1016/j.engstruct.2017.01.013.

[38] Piran Aghl P, Naito CJ, Riggs HR. Estimation of demands resulting from inelastic axial impact of steel debris. Eng Struct 2015;82:11–21. https://doi.org/10.1016/j.engstruct.2014.10.021.

[39] Piran Aghl P, Naito CJ, Riggs HR. Full-Scale Experimental Study of Impact Demands Resulting from High Mass, Low Velocity Debris. J Struct Eng 2014;140: 04014006. https://doi.org/10.1061/(asce)st.1943-541x.0000948.

[40] Pluijm R. Out-of-plane bending of masonry: behaviour and strength. Technische Universiteit Eindhoven 1999. https://doi.org/10.6100/IR528212.

[41] Postacchini M, Zitti G, Giordano E, Clementi F, Darvini G, Lenci S. Flood impact on masonry buildings: The effect of flow characteristics and incidence angle. J Fluids Struct 2019;88:48–70. https://doi.org/10.1016/j.jfluidstructs.2019.04.004.

[42] Qi ZX, Eames I, Johnson ER. Force acting on a square cylinder fixed in a free-surface channel flow. J Fluid Mech 2014;756:716–27. https://doi.org/10.1017/jfm.2014.455.

[43] Rafsanjani SH, Lourenço PB, Peixinho N. Implementation and validation of a strain rate dependent anisotropic continuum model for masonry. Int J Mech Sci 2015;104:24–43. https://doi.org/10.1016/j.ijmecsci.2015.10.001.

[44] Ruffini G, Briganti R, Girolamo P. de, Stolle J, Ghiassi B, Castellino M. Numerical Modelling of Flow-Debris Interaction during Extreme Hydrodynamic Events with DualSPHysics-CHRONO. Appl Sci. 2021, Vol. 11, Page 3618 11, 3618. https://doi.org/10.3390/APP11083618.

[45] Scacco J, Ghiassi B, Milani G, Lourenço PB. A fast modelling approach for numerical analysis of unreinforced and FRCM reinforced masonry walls under out-of-plane loading. Compos B Eng 2020;180: https://doi.org/10.1016/j.compositesb.2019.107553.

[46] Shoji G, Shimizu H, Koshimura S, Estrada M, Jimenez C. Evaluation of Tsunami wave loads acting on walls of confined-masonry-brick and concrete-block houses. J Disaster Res 2014;9(6):976–83.

[47] Silva LC, Lourenço PB, Milani G. Rigid block and spring homogenized model (HRBSM) for masonry subjected to impact and blast loading. Int J Impact Eng 2017;109:14–28. https://doi.org/10.1016/j.ijimpeng.2017.05.012.

[48] Soleimankhani H, Carozza S, Aronica GT, Jalayer F, Recupero A, Lang M, et al. Analytic Back Calculation of Debris Flow Damage Incurred to a Masonry Building: The Case of Scaletta Zanclea 2009 Event. E3S Web of Conferences 2016;7:04007.

[49] Thompson V, Dunstone NJ, Scaife AA, Smith DM, Slingo JM, Brown S, Belcher SE. High risk of unprecedented UK rainfall in the current climate. Nat Commun. 2017; 8:1 8, 1–6. https://doi.org/10.1038/s41467-017-00275-3.

[50] Wosatko A, Winnicki A, Polak MA, Pamin J. Role of dilatancy angle in plasticity-based models of concrete. Arch Civil Mech Eng 2019;19(4):1268–83.

[51] Ruffini G, Domínguez JM, Briganti R, Altomare C, Stolle J, Crespo AJC, et al. MESH-IN: A MESHed INlet offline coupling method for 3-D extreme hydrodynamic events in DualSPHysics. Ocean Engineering 2023;268:113400. https://doi.org/10.1016/j.oceaneng.2022.113400.